TU Delft

Delft University of Technology

On the performance of the helix wind farm control approach in the conventionally neutral atmospheric boundary layer

Taschner, E.; Van Vondelen, A. A.W.; Verzijlbergh, R.; Van Wingerden, J. W.

DOI
10.1088/1742-6596/2505/1/012006

Publication date
2023

Document Version
Final published version

Published in
Journal of Physics: Conference Series

Citation (APA)
Taschner, E., Van Vondelen, A. A. W., Verzijlbergh, R., & Van Wingerden, J. W. (2023). On the performance of the helix wind farm control approach in the conventionally neutral atmospheric boundary layer. *Journal of Physics: Conference Series*, *2505*(1), Article 012006. https://doi.org/10.1088/1742-6596/2505/1/012006

Important note
To cite this publication, please use the final published version (if applicable).
Please check the document version above.

Copyright
Other than for strictly personal use, it is not permitted to download, forward or distribute the text or part of it, without the consent of the author(s) and/or copyright holder(s), unless the work is under an open content license such as Creative Commons.

Takedown policy
Please contact us and provide details if you believe this document breaches copyrights.
We will remove access to the work immediately and investigate your claim.

This work is downloaded from Delft University of Technology.
For technical reasons the number of authors shown on this cover page is limited to a maximum of 10.

Journal of Physics: Conference Series

PAPER • OPEN ACCESS

On the performance of the helix wind farm control approach in the conventionally neutral atmospheric boundary layer

To cite this article: E Taschner *et al* 2023 *J. Phys.: Conf. Ser.* **2505** 012006

View the article online for updates and enhancements.

You may also like

- An initial study into the potential of wind farm control to reduce fatigue loads and extend asset life
Matt Harrison, Ervin Bossanyi, Renzo Ruisi et al.
- Response characteristics for thermal and pressure devices commonly used for monitoring nasal and oral airflow during sleep studies
J M Gehring, J-G Cho, J R Wheatley et al.
- Improving the information content of seismic data and increasing the depth of investigation by choosing the optimal length of the amplitude adjustment operator
T R Akhmedov, A M Mamedova and A A Mamedov

This content was downloaded from IP address 154.59.124.113 on 17/07/2023 at 12:54

On the performance of the helix wind farm control approach in the conventionally neutral atmospheric boundary layer

E Taschner[1], AAW van Vondelen[1], R Verzijlbergh[2,3] and JW van Wingerden[1]

[1] Delft Center for Systems and Control, Delft University of Technology, 2628 CD Delft, The Netherlands
[2] Faculty of Technology, Policy and Management, Delft University of Technology, 2628 BX Delft, The Netherlands
[3] Whiffle Weather Forecasting, 2629 JD Delft, The Netherlands

E-mail: e.taschner@tudelft.nl

Abstract. The performance of wind farms can substantially increase when their individual turbines deviate from their own greedy control strategy and instead also take into account downstream turbines operating in the wake. The helix approach is a recently introduced dynamic wind farm control strategy that tackles this issue by leveraging individual pitch control to accelerate wake recovery. Its effective implementation requires detailed knowledge about the scaling between control input and the resulting power gain and turbine loading across the farm. In the present work this scaling is explored by means of large-eddy simulation of a two-turbine farm in the conventionally neutral atmospheric boundary layer. A parameter sweep for the amplitude of the helix is performed showing monotonous increase of the farm's power output with increasing pitch amplitude within the considered range of zero to six degrees. The scaling of the power gain suggests that a threshold amplitude should be exceeded for effective speed-up of the wake recovery, whereas the damage equivalent loads computed for the turbines indicate an upper limit for the amplitude despite increasing power gains.

1. Introduction

Wind turbines are commonly clustered in farms to allow for cost-effective power extraction, as e.g. cabling, maintenance, and installation costs can be shared. However, this clustering implies an inherent coupling between turbines due to wake interaction, which renders conventional control approaches optimizing isolated turbine performance suboptimal on wind farm level. As a result, wind farm control approaches have been developed which seek to optimize the overall power extraction and turbine loading across the entire farm [1].

Recently, especially dynamic control approaches have gained attention, including dynamic induction control (DIC). Actuation signals for DIC were developed leveraging optimal control combined with large-eddy simulations (LES) [2], its physical working mechanism was studied in [3] and steps towards the practical implementation were undertaken using simplified parameterized signals [4]. These works demonstrated increased wake recovery and overall power extraction. However, significant thrust and power fluctuations were found, too [5].

Content from this work may be used under the terms of the Creative Commons Attribution 3.0 licence. Any further distribution of this work must maintain attribution to the author(s) and the title of the work, journal citation and DOI.
Published under licence by IOP Publishing Ltd

To mitigate these variations, a new dynamic control approach using individual pitch control (IPC) called the helix was introduced and benchmarked against DIC in [6]. This proof of concept showed promising gains in power extraction for the helix studying a two-turbine wind farm using LES. Nevertheless, there are still knowledge gaps regarding the impact of the helix on the flow physics in the wake, the performance in different atmospheric boundary layer (ABL) conditions and the optimal actuation signal in terms of amplitude and frequency (usually expressed as Strouhal number St) [7]. Attempts to optimize the helix signal are limited. For the initial proof of concept, the frequency is derived from DIC as $St = 0.25$ and the influence of the amplitude is analyzed for two levels [6]. A study for a single amplitude, but four different Strouhal numbers suggested that the optimal frequency might deviate from $St = 0.25$, although only considering uniform inflow [8]. In [9] reinforcement learning was applied to optimize the helix amplitude for a three-turbine wind farm ($St = 0.25$) reporting an overall power gain of 6.8%.

Looking beyond the sole optimization of the power gain, further investigations were conducted to evaluate the impact of the helix approach on turbine components. The results showed that DIC had a significant effect on the turbine tower compared to the helix approach, while the difference between both methods on the blades was minimal [10]. Another work performed a more comprehensive sensitivity analysis and found that the tower fore-aft, blade flapwise, and pitch bearing are particularly sensitive to a high-amplitude helix actuation signal, while other components are less affected [11]. Since the performance increase of the helix approach becomes more significant with amplitude, a balance should be found between the increased load and power gains. As of yet, no study has explicitly examined the amplitude scaling of power increase versus load increase for a two-turbine set-up.

The objective of the present work is therefore to obtain a more detailed insight into the amplitude scaling by conducting a parameter sweep using LES of a two-turbine farm. In terms of atmospheric conditions, we focus on the neutral ABL and in particular its most common type in the atmosphere: the conventionally neutral atmospheric boundary layer (CNBL) [12]. This study thereby informs future research on the optimal actuation signal and provides a baseline for the assessment of the amplitude-power gain scaling in different atmospheric conditions.

2. Methodology

This section outlines the methodology to simulate the flow in the ABL and the wind turbine dynamics. Further, the helix controller and the approach for the load analysis are introduced.

2.1. AMR-Wind and OpenFAST

The flow in the ABL is modeled using the LES code AMR-Wind [13]. AMR-Wind solves the filtered incompressible Navier-Stokes equations where the subgrid-scale stresses are modeled using the kinetic energy one-equation turbulence model [14]. The code uses the Boussinesq approximation in order to include the effect of density gradients on buoyancy. At the lower boundary a wall shear stress model using Monin-Obukhov similarity theory is employed following [14]. At the top of the domain, a slip wall is specified for the velocity and a fixed gradient for the potential temperature. AMR-Wind solves the governing equations on Cartesian block-structured grids, which can be locally refined either statically or dynamically. More details on the numerical implementation of AMR-Wind can be found in the work of [15], which examined the stable northeastern United States marine boundary layer. AMR-Wind further provides a coupling to OpenFAST which is used in this work and was previously employed to evaluate the performance of wind farms operating in low-level jet events [16].

OpenFAST is a multi-physics wind turbine simulation tool capable of simulating the entire wind turbine including its structural, hydro-, aero- and control dynamics [17]. In this study, the OpenFAST model for the fixed-bottom monopile variant of the IEA-15 MW turbine is

employed [18], which is representative of the next generation of offshore turbines. OpenFAST is coupled to the LES simulation using a standard actuator line model (ALM) [19].

2.2. Turbine controller

The control actions are implemented using the reference open-source controller (ROSCO) [20], where the IPC routine of ROSCO is extended to include the additional pitch actuation required for the helix. The key idea of the helix is to impose slowly periodically varying tilt and yaw moments on the turbine, thereby deflecting the wake in a helical shape and facilitating wake recovery [6]. The signals for these moments are designed in the turbine's non-rotating blade coordinate system using the corresponding yaw $\beta_{yaw}(t)$ and tilt $\beta_{tilt}(t)$ pitch angles. They are given by the relations $\beta_{tilt} = \beta \sin(\omega_e t)$ and $\beta_{yaw} = \beta \sin(\omega_e t + \psi)$, where β is the pitch amplitude and the actuation frequency $\omega_e = 2\pi f_e$ can be expressed as non-dimensional Strouhal number $St = f_e D/u_H$. The rotor diameter is denoted as D and u_H is the mean inflow wind speed at hub height. A counterclockwise (CCW) helix is obtained for a phase offset of $\psi = \pi/2$, whereas a clockwise (CW) helix results from the offset $\psi = -\pi/2$. For the implementation on the actual turbine the designed signals still have to be transformed to three blade pitch actuation signals $\beta_i(t)$ $(i = 1, 2, 3)$ expressed in the rotating blade-attached coordinate system using the inverse Multi-Blade Coordinate transform (MBC) [21]. The frequency of the resulting pitch actuation signals for a CCW helix is then given by $\omega_\beta = \omega_r + \omega_e$ $(\omega_e \ll \omega_r)$ for a wind turbine operating in below-rated conditions with constant rotor speed ω_r and collective pitch $\beta_0 = 0$ [6].

2.3. Fatigue analysis

Fatigue is a type of damage that occurs in structures as a result of repeated loading over time. This damage typically manifests as small cracks that gradually grow until the structure fails. The magnitude of the response to cyclic loading is governed by structural parameters such as damping and natural frequencies, which means that knowing these parameters is essential for designing structures such as wind turbines that must withstand cyclic loading for extended periods [22]. In the next paragraphs, the two measures for fatigue used in this study are presented: the damage equivalent load (DEL), and pitch bearing damage (PBD).

2.3.1. Damage equivalent load One way to model the damage caused by cyclic loading on a structure is through the use of the S-N (or Wöhler) curve, which indicates the number of cycles a structure can endure before failure for a given stress level [23]. The slope of the S-N curve is specific for each type of structure and is used to calculate the damage equivalent load (DEL), which condenses the total fatigue damage experienced by a structure to a single number. To use the S-N curve, it is necessary to have information on the ranges and frequencies of the different load cycles, which can be collected from a load signal using rainflow counting. The means of these cycles must then be corrected to a single mean value using the Goodman correction, which is given by:

$$A_i^{\mathrm{RF}} = A_i * ((A^{\mathrm{u}} - |A^{\mathrm{fm}}|)/(A^{\mathrm{u}} - |A_i^{\mathrm{m}}|)) \tag{1}$$

where A_i^{RF} is the Goodman-corrected range, A_i is the range, A^{m} is the mean of the i-th cycle, A^{u} is the ultimate load, and A^{fm} is the fixed mean load, which is set as the mean of the entire signal. The DEL is then calculated using the following formula:

$$DEL = ((\sum_{i=1}^{N} (A_i^{\mathrm{RF}})^m * n_i)/n_{eq})^{\frac{1}{m}} \tag{2}$$

where N is the total number of cycles, m is the inverse Wöhler slope (conventionally taken as 5 for the tower and 10 for the blades), n_i is the number of cycles with range A_i, and n_{eq} is

the equivalent cycle, which is set as 1. The calculations were performed using NREL's MLife toolbox [24]. Furthermore, the DELs in this work are calculated for the blade root (BR) moment (edgewise, flapwise, and torsional direction), the tower top (TT) moment (fore-aft, side-side, and torsional direction) and the tower base (TB) moment (fore-aft and side-side direction). The computational expense of AMR-Wind simulations limits the loads analyses performed in this work to 35 minutes of suitable simulation data for DEL calculation. This is less than a typical loads analysis, which uses either six 10-minute datasets with different turbulence seeds or a single 1-hour dataset [25]. The fatigue results presented in this work should therefore be considered as preliminary.

2.3.2. Pitch bearing damage Pitch bearings accumulate damage differently due to their dynamic character [26]. Fatigue develops in radial positions on the bearing rings due to movement and the blade moment acting on the bearing. Both these components are taken into account in the pitch bearing damage (PBD) calculation, which differs from the conventional DEL. The standard used in this study is one prescribed by bearing manufacturers and given by the following equation:

$$PBD(\phi) = \sum_{k=1}^{N} \delta\theta(k)(\max(\cos(\phi)M_{\text{flap}}(k) + \sin(\phi)M_{\text{edge}}(k), 0))^m, \tag{3}$$

where k denotes the OpenFAST time step, $\delta\theta$ is the pitch difference, ϕ is the radial position of the inner bearing on the outer ring, M_{flap} is the flapwise blade root bending moment, M_{edge} is the edgewise blade root bending moment, and m is the inverse Wöhler slope, taken here as 3. In our analysis, the radial position with the largest damage is considered.

3. Setup of the numerical simulations

This section presents the setup of the precursor simulation which generates a developed turbulent ABL state and the subsequent turbine simulations which use this state as initial condition.

3.1. Precursor simulation

A CNBL including Coriolis forces is considered for the precursor where the ABL flow develops against a stably stratified free atmosphere with lapse rate $\gamma = 1\,\text{K/km}$. A capping inversion is employed to control the growth and height of the CNBL [27]. For the present study a boundary layer height of $h = 1000\,\text{m}$ and a surface roughness of $z_0 = 0.0002\,\text{m}$ are considered. The value of the surface roughness is in agreement with offshore measurements made off the Dutch coast [28] and the latitude is chosen accordingly as $\phi_{lat} = 52.6°$. Furthermore, a controller is used to drive the flow at turbine hub height ($z_H = 150\,\text{m}$) to a wind speed of $u_H = 10\,\text{m/s}$ and a direction of $\phi = 90°$ aligned with the eastern direction (aligned with the x-axis of the rectangular domain). This choice places the operating point of the first-row turbine close to the upper limit of the below-rated control regime, where collective pitch control is still disabled.

The velocity profile is initialized with the desired hub velocity u_H. Further, the initialization of the temperature profile is crucial to obtain the desired boundary layer height. The height of the inversion determines the point up to which the boundary layer can grow before its growth is restricted by the negative buoyancy forces in the inversion layer. The equilibrium strength for the capping inversion can be estimated as $h = A\theta_0 u_*^2/(g\Delta\theta)$ where $A \approx 500$ is a constant and $\Delta\theta$ is the inversion strength [29]. One can obtain the minimum required strength $\Delta\theta_{min}$ for equilibrium using a typical value for the friction velocity in offshore conditions $u_* = 0.28\,\text{m/s}$ [30] and a reference potential temperature of $\theta_0 = 288.15\,\text{K}$. The implemented inversion strength is

then chosen as $\Delta\theta = 2.5K \approx 2\Delta\theta_{min}$. The complete temperature initial condition is designed using the function

$$\theta(z) = \theta_m + a\frac{\tanh(\eta)+1}{2} + b\frac{\ln[2\cosh(\eta)]+\eta}{2}, \tag{4}$$

where $\eta = (z-l)/(c\Delta h)$ is a non-dimensional height, $\Delta h = 100\,\mathrm{m}$ is the inversion depth, $\theta_m = \theta_0 = 288.15\,\mathrm{K}$ is the potential temperature in the mixed layer and the parameters a, b, c and l are directly related to the inversion characteristics [31].

The domain size for the precursor simulation is $L_x = 4160\,\mathrm{m}$, $L_y = 3200\,\mathrm{m}$ and $L_z = 1600\,\mathrm{m}$ required to accommodate two turbines and limit domain blockage. The domain is discretized with an isotropic grid of size $\Delta x = 10\,\mathrm{m}$ which is in agreement with requirements for the CNBL [32, 33]. Using periodic boundary conditions in the horizontal directions (x and y) the flow is advanced for 16 hours to allow for the development of a quasi-stationary turbulent ABL state [34]. During the subsequent 45 minutes, instantaneous y-z planes are sampled at the inflow $x = 0\,\mathrm{m}$ which are then stored as inflow boundary conditions for the turbine simulations.

3.2. Turbine simulations

The small wind farm considered here consists of two IEA-15 MW turbines located at $x = 5D$ and $x = 10D$ from the inflow each centered at $y = L_y/2$ in the domain. The grid around the two turbines and their wakes is refined to $\Delta x = 5\,\mathrm{m}$ in a box of size $L_{x,r} = 3840\,\mathrm{m}$, $L_{y,r} = 960\,\mathrm{m}$ and $L_{z,r} = 600\,\mathrm{m}$ starting $4.5D$ upstream of the first turbine. In terms of rotor diameter the resolution is $D/\Delta x = 48$ which allows for the use of the ALM. The simulation is advanced in time for 45 minutes using a constant time step of $\Delta t_{LES} = 0.025\,\mathrm{s}$ which ensures that the tips of the blades pass less than one grid cell per time step. The boundary condition in the y-direction is still periodic whereas in the x-direction an inflow/outflow boundary condition based on the recorded precursor data is applied in order to avoid the re-circulation of the wakes.

The OpenFAST simulation uses a time step of $\Delta t_{OF} = 0.005\,\mathrm{s}$ and active degree of freedoms for generator, blades, tower and platform. The blades, tower and nacelle are represented with $N_B = 60/N_T = 72/N_N = 1$ actuator points, respectively, and the force projection onto the LES grid is done with a Gaussian kernel of width $\epsilon = 2\Delta x = 10\,\mathrm{m}$.

Using the outlined setup, the parameter sweep for the pitch amplitude is performed considering the six cases $\beta \in \{0, 1, 2, 3, 4, 6\}^\circ$ (denoted as BL, HL1, ...) to explore the full range of dynamics. It should be noted that the default pitch rate limits of the IEA-15 MW turbine have to be increased if $\beta > 4^\circ$ in order to enable helix pitch actuation. All helix cases in this study use the most common helix actuation frequency of $St = 0.25$, but we do note that there is still uncertainty not only in the optimal amplitude but also frequency [8]. Note that the helix is only implemented for the upstream turbine (denoted as T1).

4. Results

This section first presents the characteristics of the precursor simulation. Subsequently, it is shown how the different helix actuation signals alter the turbine wake and the response of the turbines in terms of wake development, power extraction and loading.

4.1. Precursor simulation

The characteristics of the precursor simulation are shown in Figure 1, where the data is averaged across the time interval used as the inflow boundary condition for the turbine runs. As can be seen from the vertical wind speed profile, the wind controller successfully ensures a hub height wind speed of $u_H = 10\,\mathrm{m/s}$. The local shear exponent defined as $\alpha = (z/u_{horiz})(du_{horiz}/dz)$ resulting from the wind speed profile is in the range of $\alpha = 0.07 - 0.085$ across the rotor except close to the bottom edge of the rotor disk where it reaches up to $\alpha = 0.11$. The veer profile is

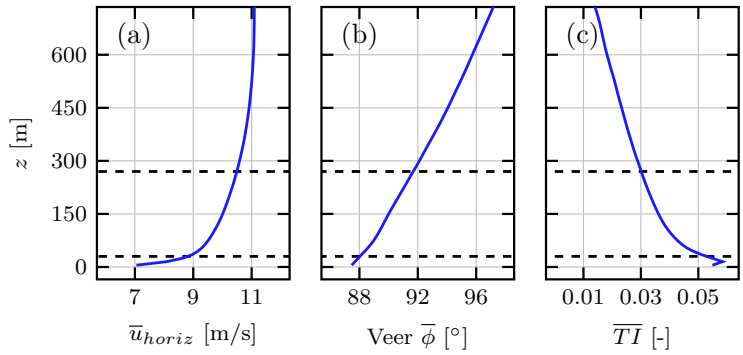

Figure 1. Vertical mean profiles of horizontal velocity magnitude (a), veer (b) and turbulence intensity (c) averaged across horizontal planes and the 45 minutes of the precursor inflow data. The rotor region is marked with dashed horizontal lines.

nearly linear in the lower part of the ABL leading to a wind direction change of $\Delta\phi = 3.8°$ across the rotor. The turbulence intensity is defined as $TI = (\frac{1}{3}\overline{u_i'u_i'}/\overline{u_iu_i})^{0.5}$ (where $u_i' = u_i - \overline{u}_i$ denotes the fluctuation around the temporal average and we use the Einstein summation convention) [5]. It reaches maximum values at the wall where turbulence is generated due to shear and decays with increasing height. The inflow TI level experienced by the rotor spans from 3% at the rotor top to 5.3% at the rotor bottom. The mean friction velocity is $u_* = 0.2855\,\mathrm{m/s}$, which closely matches the value assumed for the calculation of the inversion strength.

4.2. Turbine simulations: Wake development

The key concept of the helix control approach is to enhance the recovery of the wake behind the turbine. This is illustrated by comparing the vertical mean streamwise velocity profiles in the wake of turbine T1 for the baseline case and different helix signals (Figure 2). The mean profiles and quantities in the remainder of this article are obtained by averaging across the last 35 minutes of the simulation time discarding the first transient 10 minutes of turbine start-up.

The initial wake behind the turbine consists of two regions of large velocity deficit separated by a low deficit region in the proximity of the nacelle. The deficit is superposed onto the incoming shear profile and during its downstream development the low deficit footprint of the nacelle diffuses. At $x/D = 3$ it is only visible for the BL and HL1 cases. There is a monotonous trend of larger helix pitch amplitudes leading to faster recovery of the wake, although differences between the BL and HL1 cases are minimal. We quantify the comparison by computing the relative increase of mean streamwise power integrated across the rotor area. At $x/D = 4$ the relative increase in power is 5.1% for the HL1 case, whereas the cases HL2, HL3, HL4 and HL6 lead to an increase of 16.2%, 29.3%, 48.8% and 86.6%, respectively.

The main trend found for the vertical mean velocity profiles also transfers to the turbulence

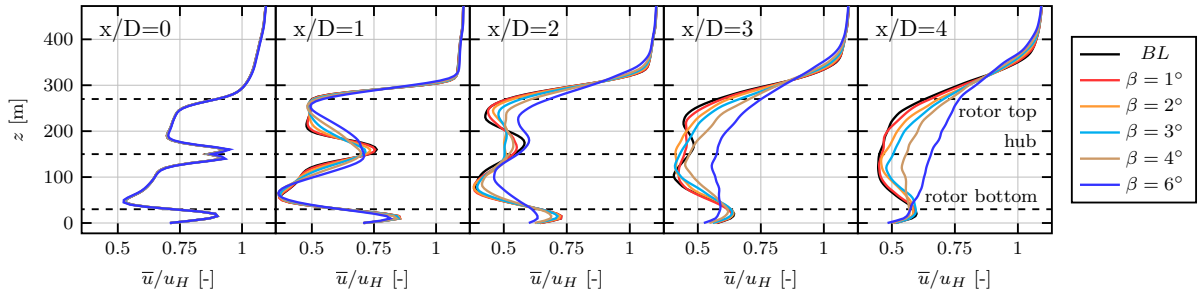

Figure 2. Vertical mean streamwise velocity profiles at the location of turbine T1 ($x/D = 0$) and four locations downstream in its wake. Note that at $x/D = 0$ all lines overlap.

kinetic energy $\overline{k}_{res}$ (TKE), where only the part directly resolved by the LES is considered (Figure 3). Higher helix pitch amplitudes lead to larger TKE levels at a fixed streamwise location. For all cases, the TKE level is especially elevated in the region of the upper and lower rotor tip and the nacelle region. However, for larger values of the pitch amplitude, the TKE level also saturates earlier upstream. Further downstream at $x/D = 4$ this leads to similar TKE levels at the upper edge of the rotor region for all cases including the baseline. Within the rotor region, there are still differences between the BL and HL6 cases of up to 300%.

We further compare the cases by analyzing the wake meandering behavior. The instantaneous wake centers in y-z planes are computed using the streamwise momentum deficit following [35]

$$y_c(t) = \frac{\int \Delta u^2(t,y,z) y \, dydz}{\int \Delta u^2(t,y,z) \, dydz}, \quad z_c(t) = \frac{\int \Delta u^2(t,y,z) z \, dydz}{\int \Delta u^2(t,y,z) \, dydz} \tag{5}$$

where $\Delta u(t,y,z) = u_{inflow}(y,z) - u(t,y,z)$ is the velocity deficit and the inflow is taken at $x = -2D$ upstream of T1. Using the mean wake centers $(\overline{y}_c, \overline{z}_c)$ as the origin of a polar coordinate system the instantaneous wake centers are transformed to a radius $r_c(t)$ and angle $\gamma_c(t)$. Binning the angles into bins of size 15° and computing the average radius per bin results in the mean wake center displacements $\overline{r}(\gamma)$ shown in Figure 4. Larger helix actuation amplitudes lead to larger vertical and horizontal wake center displacement throughout the wake.

4.3. Turbine simulations: Turbine response

It is now studied how the trend of enhanced wake recovery with increasing helix pitch amplitude impacts the generated power of the farm (Figure 5 (a)). The second turbine's and the farm's cumulated power gain increase monotonously with β and interestingly scale superlinear for $\beta \in (0,2)°$. It should be noted that even though the inflow wind speed for the upstream turbine is chosen close to the upper limit of the region II control regime the second turbine still

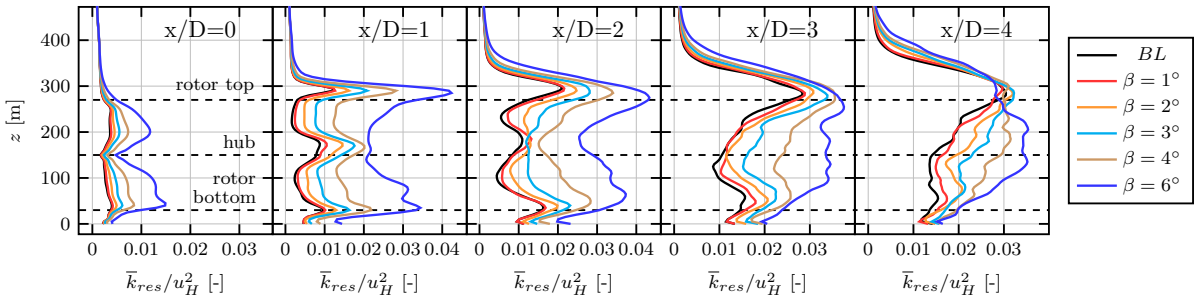

Figure 3. Vertical mean profiles of resolved turbulence kinetic energy at the location of turbine T1 ($x/D = 0$) and four locations downstream in its wake.

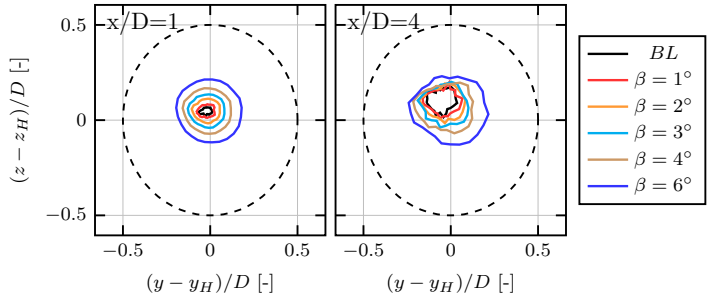

Figure 4. Binned mean wake center displacement $\overline{r}(\gamma)$ around the mean wake center $(\overline{y}_c, \overline{z}_c)$ in the wake of T1 at $x/D = 1$ and $x/D = 4$. The dashed line indicates the extent of the rotor. The axes are centered around the turbine's hub position.

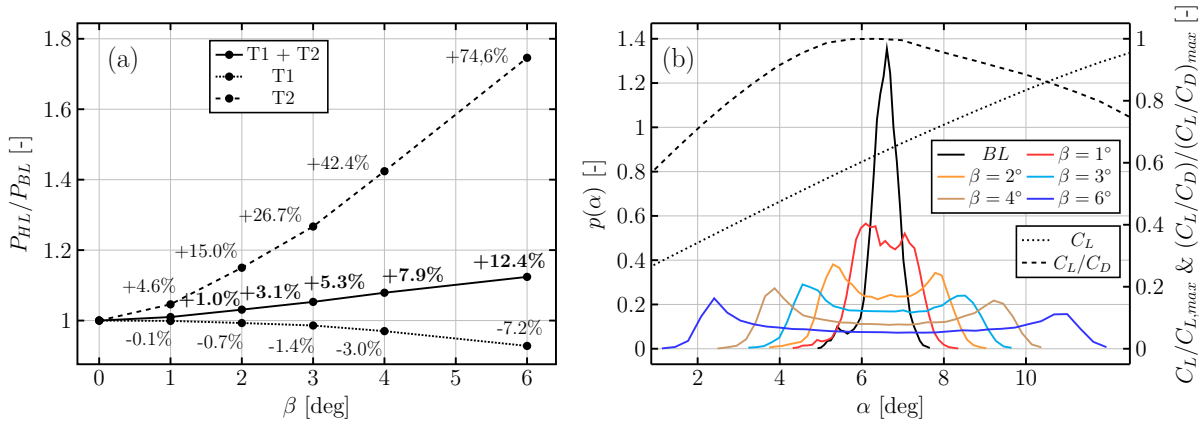

Figure 5. Relative power gain for the two-turbine wind farm with respect to the BL case (a) and PDF (normalized such that the respective integral equals unity) of the angle of attack for a blade section at 87% of the span (b). The dotted and dashed lines indicate the airfoil's lift coefficient and lift-to-drag ratio normalized with their maximum values, respectively.

operates partially in control regime 1.5. In this regime, the turbine ensures that a minimum rotor speed constraint is fulfilled by collectively pitching the blades, but the achievable power coefficient is still lower than in region II. The time spent in region 1.5 increases with decreasing β. Nevertheless, the superlinear scaling is not the sole artefact of the change of control regimes since the above-reported increase in streamwise kinetic energy at $x/D = 4$ scales similarly to the power gain at T2. These results suggest that there is a threshold amplitude $\beta \approx 1° - 2°$, which should be exceeded in order to reach the more linear scaling regime of the cumulated power gain and thus fully capitalizes on the helix actuation at T1.

We also explore the upper end of the β range, although these values are likely higher than the values which can be implemented in practice. Relative power losses at T1 become especially relevant for $\beta > 3°$ but are still compensated for by the power gain at T2. The relative power gains are of the same order as literature results (DTU-10 MW turbine and $TI = 5\%$) that reported power gains of 3.4% ($\beta = 2.5°$) and 7.5% ($\beta = 4.0°$) using the same St [6].

The impact of the helix actuation on the local aerodynamics at a blade section at 87% of the span is visualized in Figure 5 (b). It shows the probability density functions (PDFs) for the angle of attack and in addition the $\alpha - C_L$ & $\alpha - (C_L/C_D)$ characteristics of the airfoil. For the BL case the airfoil is mainly operating in proximity of the optimal lift-to-drag ratio. For the largest pitch amplitude $\beta = 6°$ the angle of attack still does not reach the airfoil's static stall limit. However, the airfoil mostly operates in regions of suboptimal lift-to-drag ratio reaching values as low as $(C_L/C_D) = 0.6(C_L/C_D)_{max}$ for the HL6 case.

When judging the effectiveness of the helix approach aerodynamic performance cannot be considered in isolation. The turbine loading of both the upstream and downstream turbines has to be taken into account. Figure 6 shows the power spectral densities (PSDs) of the out-of-plane blade moments (MOoPs) for T1 and T2. At T1 there is a strong peak visible at the 1P+St frequency which is the helix pitch actuation frequency for a CCW helix in the rotating blade-attached coordinate system. At the downstream turbine T2, the comparison between the baseline and the helix cases shows that the upstream helix actuation still leaves a detectable footprint at the frequency of $St = 0.25$. The load impact of the helix on T1 and T2 can be quantitatively compared by computing the DEL for blades/tower and the PBD (Figure 7). The figure shows a trend of increased loading as amplitude increases for T1. Especially the blade root flapwise, tower top fore-aft, tower torsional, and pitch bearing damage are sensitive to increased

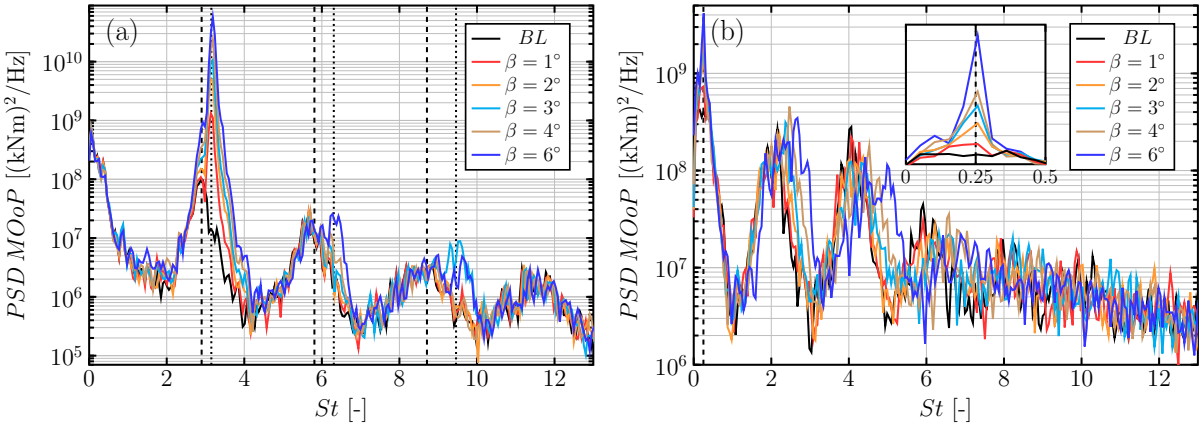

Figure 6. PSD of the MOoPs measured at the first blade of T1 (a) and T2 (b). In plot (a) dashed lines denote the 1P, 2P and 3P frequencies of the BL case and dashed lines the 1P+St, 2P+2St and 3P+3St frequencies. In plot (b) the dashed line indicates $St = 0.25$.

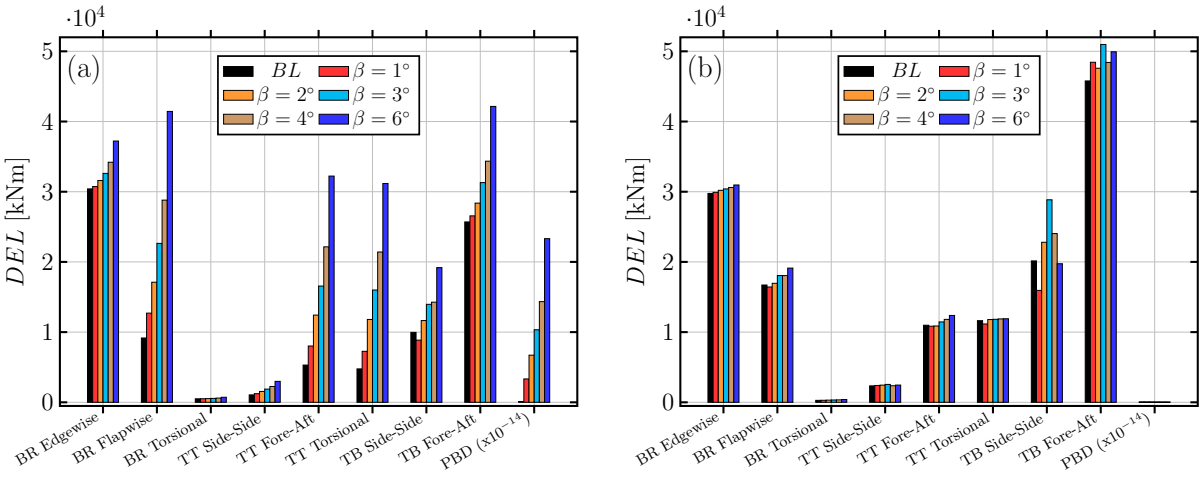

Figure 7. Damage equivalent loads and pitch bearing damage for T1 (a) and T2 (b). Note that the PBD is scaled with a factor of 10^{-14} to fit in the figure.

amplitude, which aligns with previous research [11]. Interestingly, the downstream turbine does not seem significantly impacted by the helical-shaped wake, experiencing only slight increases in loading. This might also be explained due to the higher effective wind speed on the downstream turbine as a result of the faster wake recovery due to the helix.

5. Conclusions

In this study we analyzed the performance of the helix wind farm control approach for a two-turbine farm operating in the CNBL. A parameter sweep was conducted for the pitch amplitude considering a CCW helix with $St = 0.25$. There was no saturation of the power gain detected within the considered range of pitch amplitudes. However, the DELs at the upstream turbine were sensitive to the helix actuation signal, thus imposing an upper limit for the actuation. A lower limit is suggested by the very small power gain found for $\beta = 1°$. Therefore, the helix actuation amplitude should be chosen as a careful trade-off between the scaling of power gain and loading with β. Future work will focus on assessing how the power gain curve is affected by

different ABL conditions, the optimization of the actuation Strouhal number and a more robust calculation of the DEL using multiple turbulence seeds.

Acknowledgments

This work is part of the Hollandse Kust Noord wind farm innovation program where CrossWind C.V., Shell, Eneco and Siemens Gamesa are teaming up; funding for the PhDs was provided by CrossWind C.V. and Siemens Gamesa. We further would like to thank Dries Allaerts for his advice on the CNBL and acknowledge the computing resources provided by DelftBlue [36].

References

[1] Meyers J, Bottasso C, Dykes K, Fleming P, Gebraad P, Giebel G, Göçmen T and van Wingerden J W 2022 *Wind Energy Science* **7** 2271–2306
[2] Yılmaz A E and Meyers J 2018 *Physics of Fluids* **30** 085106
[3] Croce A, Cacciola S, Montero Montenegro M, Stipa S and Praticó R 2023 *Wind Energy* **26** 325–343
[4] Munters W and Meyers J 2018 *Wind Energy Science* **3** 409–425
[5] van der Hoek D, Frederik J, Huang M, Scarano F, Simao Ferreira C and van Wingerden J W 2022 *Wind Energy Science* **7** 1305–1320
[6] Frederik J A, Doekemeijer B M, Mulders S P and van Wingerden J W 2020 *Wind Energy* **23** 1739–1751
[7] Houck D R 2021 *Wind Energy* **25** 195–220
[8] Muscari C, Schito P, Viré A, Zasso A, van der Hoek D and van Wingerden J W 2022 *J. Phys.: Conf. Series* **2265** 022057
[9] Korb H, Asmuth H, Stender M and Ivanell S 2021 *J. Physics: Conf. Series* **1934** 012022
[10] Frederik J A and van Wingerden J W 2022 *Renewable Energy* **194** 582–595
[11] van Vondelen A A W, Navalkar S T, Kerssemakers D R H and van Wingerden J W 2023 *American Control Conference (ACC)* (San Diego, California, USA: AACC)
[12] Zilitinkevich S S and Esau I N 2002 *Boundary-Layer Meteorology* **104** 371–379
[13] `https://github.com/Exawind/amr-wind`
[14] Moeng C H 1984 *Journal of the Atmospheric Sciences* **41** 2052–2062
[15] Cheung L, Brazell M J, Hsieh A, Ananthan S, Vijayakumar G and deVelder N 2021 *AIAA Scitech 2021 Forum* (Virtual Event: American Institute of Aeronautics and Astronautics)
[16] Chatterjee T, Li J, Yellapantula S, Jayaraman B and Quon E 2022 *J. Phys.: Conf. Series* **2265** 022004
[17] Jonkman J 2013 *51st AIAA Aerospace Sciences Meeting including the New Horizons Forum and Aerospace Exposition* (Grapevine, Texas, USA: AIAA)
[18] `https://github.com/IEAWindTask37/IEA-15-240-RWT/tree/master/OpenFAST/IEA-15-240-RWT-Monopile`
[19] Sørensen J N and Shen W Z 2002 *Journal of Fluids Engineering* **124** 393–399
[20] Abbas N J, Zalkind D S, Pao L and Wright A 2022 *Wind Energy Science* **7** 53–73
[21] Bir G 2008 *46th AIAA Aerospace Sciences Meeting and Exhibit* (Reno, Nevada, USA: AIAA)
[22] van Vondelen A A W, Navalkar S T, Iliopoulos A, van der Hoek D C and van Wingerden J W 2022 *Wind Energy Science* **7** 161–184
[23] Burton T, Jenkins N, Sharpe D and Bossanyi E 2011 *Wind energy handbook* (John Wiley & Sons)
[24] Hayman G 2012 *National Renewable Energy Laboratory, Golden, CO* **74** 106
[25] IEC 2019 Wind energy generation systems – Part 1: Design requirements for offshore wind turbines IEC 61400-3 International Energy Commission Geneva, Switzerland
[26] Stammler M, Reuter A and Poll G 2018 *Renewable Energy Focus* **25** 40–47
[27] Allaerts D and Meyers J 2015 *Physics of Fluids* **27** 065108
[28] Taylor P K and Yelland M J 2001 *Journal of Physical Oceanography* **31** 572–590
[29] Csanady G T 1974 *Boundary-Layer Meteorology* **6** 63–79
[30] Brost R A, Lenschow D H and Wyngaard J C 1982 *Journal of Atmospheric Sciences* **39** 800 – 817
[31] Rampanelli G and Zardi D 2004 *Journal of Applied Meteorology* **43** 925–933
[32] Wurps H, Steinfeld G and Heinz S 2020 *Boundary-Layer Meteorology* **175** 179–201
[33] Hsieh A S, Brown K A, deVelder N B, Herges T G, Knaus R C, Sakievich P J, Cheung L C, Houchens B C, Blaylock M L and Maniaci D C 2021 *J. Wind. Eng. Ind. Aerodyn.* **218** 104754
[34] Zilitinkevich S, Esau I and Baklanov A 2007 *Q. J. R. Meteorol. Soc.* **133** 265–271
[35] Abkar M and Porté-Agel F 2016 *Physical Review Fluids* **1** 063701
[36] Delft High Performance Computing Centre (DHPC) 2022 DelftBlue Supercomputer (Phase 1) `https://www.tudelft.nl/dhpc/ark:/44463/DelftBluePhase1`